

pubs.acs.org/JACS Article

Molecular Switch Cobalt Redox Shuttle with a Tunable Hexadentate Ligand

Austin L. Raithel, William E. Meador, Tea-Yon Kim, Richard J. Staples, Jared H. Delcamp,* and Thomas W. Hamann*



Cite This: J. Am. Chem. Soc. 2023, 145, 1367–1377



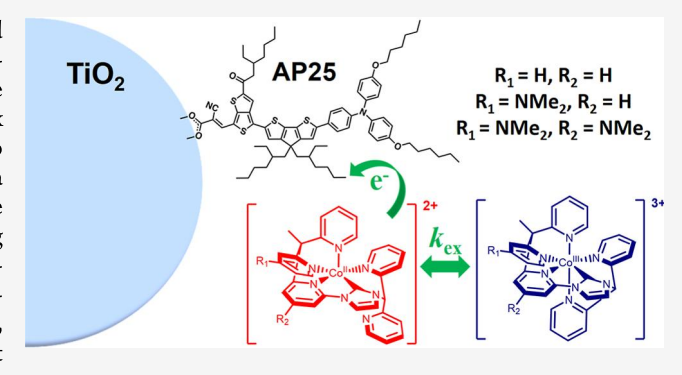
ACCESS

III Metrics & More

Article Recommendations

Supporting Information

ABSTRACT: Strong-field hexadentate ligands were synthesized and coordinated to cobalt metal centers to result in three new low-spin to low-spin Co(III/II) redox couples. The ligand backbone has been modified with dimethyl amine groups to result in redox potential tuning of the Co(III/II) redox couples from -200 to -430 mV versus $Fc^{+/0}$. The redox couples surprisingly undergo a reversible molecular switch rearrangement from five-coordinate Co(II) to six-coordinate Co(III) despite the ligands being hexadentate. The complexes exhibit modestly faster electron self-exchange rate constants of 2.2-4.2 M $^{-1}$ s $^{-1}$ compared to the high-spin to low-spin redox couple $[Co(bpy)_3]^{3+/2+}$ at 0.27 M $^{-1}$ s $^{-1}$, which is attributed to the change in spin state being somewhat offset by this coordination switching behavior. The complexes were



utilized as redox shuttles in dye-sensitized solar cells with the near-IR AP25 + D35 dye system and exhibited improved photocurrents over the $[Co(bpy)_3]^{3+/2+}$ redox shuttle (19.8 vs 18.0 mA/cm²). Future directions point toward pairing the low-spin to low-spin Co(II/III) tunable series to dyes with significantly more negative highest occupied molecular orbital potentials that absorb into the near-IR where outer sphere redox shuttles have failed to produce efficient dye regeneration.

■ INTRODUCTION

Dye-sensitized solar cells (DSSCs) remain a promising renewable power generation technology that can be produced at minimal cost with great tunability. The DSSCs are composed of sensitizer dyes to harvest photons, a mesostructured semiconductor photoanode as an electron acceptor and transport material, and redox couples to shuttle electrons (redox shuttles) from the counter electrode to the oxidized dyes in order to complete the circuit. The ability to modulate the photoanode, dye, redox shuttle, and counter electrode of the devices has allowed for gradual improvement of devices with time. Power conversion efficiencies (PCEs) up to 14% under 1 sun and 34.5% at 1000 lux intensity have been demonstrated with various dye and redox shuttle systems. The highest efficiencies have used either cobalt- or copper-based outer sphere redox systems as their electrolyte.³⁻⁷ Due to the adjustable electron donation of the ligands to the metal centers, the redox potential has been optimized to reduce the driving force for dye regeneration, enabling the highest PCE devices. The DSSCs utilizing copper and cobalt redox shuttles have primarily focused on harvesting light between 300 and 800 nm, leaving a large section of the solar spectrum unharvested and limiting the maximal efficiency attainable. Achieving PCEs closer to 20% with DSSCs will likely require harvesting photons deeper into the near-infrared (NIR, 8001100 nm). Use of photons deeper in the NIR region has largely been prevented by having suitable redox shuttles capable of dye regeneration. Realization of DSSCs producing electricity from NIR photons would also enable high-efficiency tandem devices, which are capable of achieving over 30% efficiency, to be realized. For the efficient use of NIR photons in DSSC devices, deeper-absorbing NIR dyes will require redox shuttles with more negative redox potentials while also minimizing the dye regeneration driving force needed to maximize the available open-circuit voltage.

 $[\text{Co(bpy)}_3]^{3+/2+}$ is an exceptionally high-performing outersphere redox shuttle with a near record PCE of 14.2% demonstrated in a DSSC device (Figure 1).^{6,16} However, it requires large driving forces of ≈ 0.5 V for efficient dye regeneration.¹⁷ This voltage loss is largely dictated by the considerable inner-sphere reorganization energy, λ_i , of the complex undergoing a high-spin Co(II) to low-spin Co(III) transition upon oxidation, which reduces the dye regeneration

Received: November 11, 2022 Published: January 3, 2023





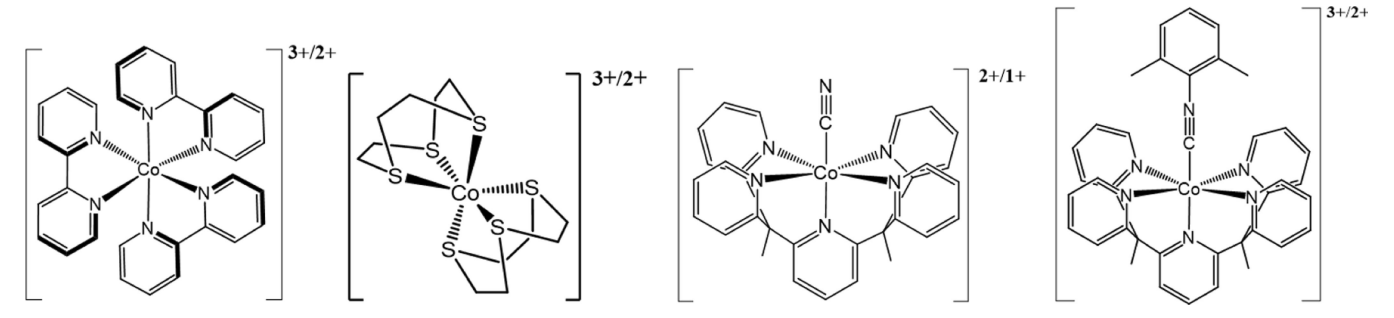


Figure 1. Molecular structures of referenced cobalt redox shuttles for DSSCs, listed from left to right: cobalt tris(2,2'-bipyridine), $[Co(bpy)_3]^{3+/2+}$, cobalt bis(1,4,7-trithiacyclononane), $[Co(ttcn)_2]^{3+/2+}$, cobalt 2,6-bis(1,1-bis(2-pyridyl)ethyl)pyridine cyanide $[Co(PYSMe_2)(CN)]^{2+/1+}$, and cobalt 2,6-bis(1,1-bis(2-pyridyl)ethyl)pyridine 2,6-dimethylphenyl isocyanide $[Co(PYSMe_2)(DMP-CN)]^{3+/2+}$.

Figure 2. (Top reaction) stepwise reaction of 2-ethylpyridine, *n*-butyllithium, 2-fluoropyridine derivative, and 2,6-difluoropyridine derivative to form compounds 1–3. (Middle reaction) reaction of 1–3 with imidazole to form compounds 4–6. (Bottom reaction) reaction of 4–6 with *bis*(2-pyridyl)bromomethane to form the ligand series compounds 7–9.

rate. 18 Our group has attempted to minimize the driving force by changing the spin state of cobalt redox shuttles by inducing low-spin Co(II) complexes. By inducing a low-spin Co(II) to low-spin Co(III) electron-transfer process, the inner-sphere reorganization energy is decreased, reducing the necessary driving force for dye regeneration. 19,20 Two of the redox shuttles [Co(ttcn)]^{3+/2+} (ttcn itrithiacyclononane) and [Co- $(PY5Me_2)$ (DMP-CN)]^{3+/2+} $[PY5Me_2, is 2,6-bis(1,1-bis(2-bis(1,1-bis(1,$ pyridyl)-ethyl)pyridine and DMP-CN is 2,6-dimethylphenyl isocyanide] showed efficient dye regeneration but still resided at redox potentials too positive for NIR sensitizers (Figure 1). In addition, the performance of $[Co(ttcn)]^{3+/2+}$ was limited by recombination, which we suggest can be improved via a combination of reducing the driving force for recombination, that is, pushing the potential negative, and increasing the reorganization energy. Another low-spin Co(II) redox shuttle, $[Co(PY5Me_2)(CN)]^{2+/1+}$, demonstrated a suitably negative redox couple but suffered from stability issues and the formation of dimer and cluster complexes in solution.²

Herein, a series of cobalt redox shuttles are synthesized with the goal of increased stability, redox potential tunability, and a strong-field ligand framework for low-spin Co(II) redox couples. Inspiration came from the PY5Me₂, PY4Im, and bpyPY4 ligands previously coordinated to cobalt.^{22–24} The PY4Im ligand induced a low-spin Co(II) complex and a more negative redox potential due to the strong sigma donation of the incorporated N-heterocyclic carbene (NHC). The bpyPY4 ligand demonstrated improved stability when coordinated to cobalt and used as a DSSC redox shuttle. To increase the stability and induce low-spin Co(II) complexes, a new hexadentate NHC carbene ligand that also allows for incorporation of dimethylamine (DMA) functional groups to adjust the redox potential is reported. This has resulted in a new series of low-spin to low-spin cobalt(III/II) redox shuttles to be paired with NIR sensitizers at more negative potentials.

EXPERIMENTAL SECTION

All chemicals and materials were obtained from commercial suppliers unless otherwise noted (MiliporeSigma, Oakwood Chemical, Alfa Aesar, Solaronix, Cambridge Isotopes, Great Cell Solar, Solaronix, and Dyenamo). All solvents used for the synthesis of compounds 1–3 and 10a–12b and the measurements of the cobalt complexes were dried

10a [Co(PY5lm)](OTf)₂ (65%), **10b** [Co(PY5lm)](OTf)₃ $R_1 = H$, $R_2 = H$ (85%)

11a [Co(PY5ImDMA1)](OTf)₂ (91%), **11b** [Co(PY5ImDMA1)](OTf)₃ $R_1 = NMe_2$, $R_2 = H$ (73%)

12a [Co(PY5ImDMA2)](OTf)₂ (67%), **12b** [Co(PY5ImDMA2)](OTf)₃ $R_1 = NMe_2$, $R_2 = NMe_2$ (82%)

Figure 3. (Top reaction) coordination of the hexadentate ligand to Co(II) triflate. (Bottom reaction) oxidation of the Co(II) complexes to Co(III) with ferrocenium triflate.

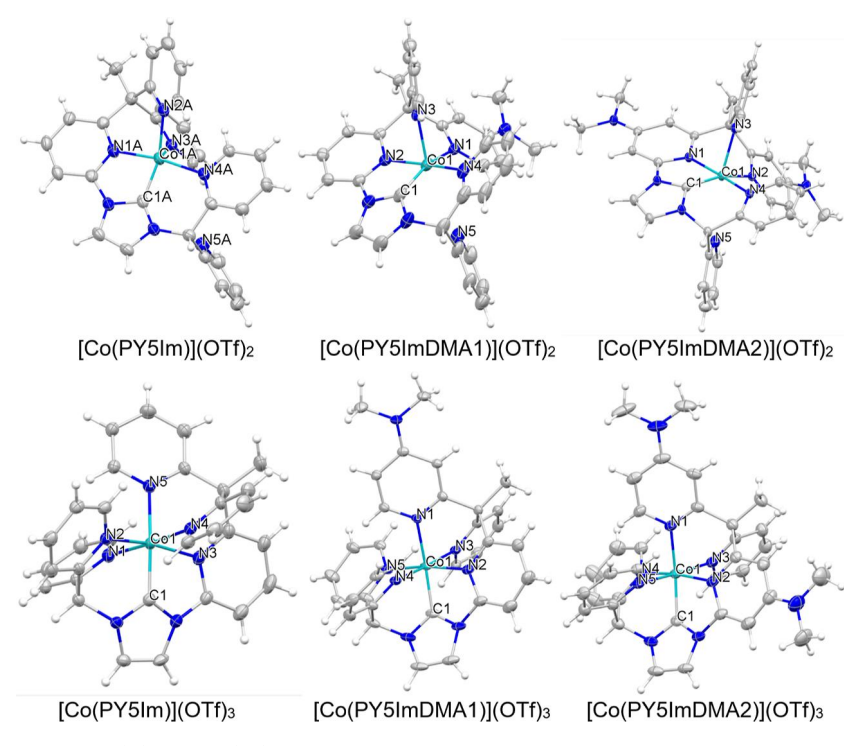


Figure 4. Crystal structures of the Co(II) and Co(III) complexes.

over activated 3 Å molecular sieves for 2 days and were then degassed using a Schlenk line before being stored in a nitrogen-filled glovebox for use. Potassium carbonate was dried for 24 h under vacuum at 100 °C before being used in the synthesis of **10a–12b**. 4-Dimethylamino-2-fluoropyridine and 4-dimethylamino-2,6-difluoropyridine were synthesized according to previously established procedures. Stromobis (2-pyridyl) methane was synthesized from 2-(2-pyridylmethyl)pyridine, both of which were synthesized from 2-(2-pyridylmethyl)pyridine, both of which were synthesized following reported procedures. Fc](OTf), [FcMe₂](OTf), [FcMe₈](OTf), and [FcMe₁₀](OTf), where Fc is ferrocene, were synthesized following a reported method in a nitrogen-filled glovebox. Detailed synthesis, characterization, and measurement details are in the Supporting Information. DSSC devices fabricated with LEG4 (3-{6-{4-[bis(2',4'-dibutyloxybiphenyl-4-yl)amino-]phenyl}-4,4-dihexyl-cy-

clopenta-[2,1-*b*:3,4-*b'*] dithiophene-2-yl}-2-cyanoacrylic acid) were fabricated following modified reported procedures.²⁰ DSSC devices fabricated with AP25 + D35 were fabricated according to a modified report. AP25 is (*E*)-3-(4-(6-(4-(*bis*(4-(hexyloxy)phenyl)amino)-phenyl)-4,4-*bis*(2-ethylhexyl)-4H-cyclopenta[2,1-*b*:3,'4-*b'*]-dithiophen-2-yl)-2-(((2-ethylhexyl)oxy)carbonyl)thieno[3,4-*b*]-thiophen-6-yl)-2-cyanoacrylic acid, and D35 is (*E*)-3-(5-(4-bis(2',4'-dibutoxy-[1,1'-biphenyl]-4-yl)amino)phenyl)thiophen-2-yl)-2-cyanoacrylic acid.¹³ The structures of LEG4, AP25, and D35 are reported in the Supporting Information (Figure S38). AP25 is prepared as previously described.¹⁰ The AP25 + D35 DSSC devices were sealed with a UV-light curing adhesive as previously described.²⁹ Details are provided in the Supporting Information. At least 10 dye-

Table 1. Metal-to-Ligand Bond Distances (Å) from Single-Crystal X-ray Diffraction Data

complex	Co-N ₁	Co-N ₂	Co-N ₃	Co-N ₄	Co-N ₅	Co-C ₁
$[Co(PY5Im)]^{2+}$	1.926(3)	1.998(3)	2.086(3)	1.973(3)	_	1.847(4)
$[Co(PY5Im)]^{3+}$	1.990(3)	1.958(3)	1.959(3)	1.952(3)	1.974(3)	1.865(3)
$[Co(PY5ImDMA1)]^{2+}$	1.9557(2)	1.9256(2)	2.073(2)	1.959(2)	_	1.830(2)
$[Co(PY5ImDMA1)]^{3+}$	1.953(2)	1.923(3)	1.938(2)	1.979(2)	1.935(3)	1.863(3)
$[Co(PY5ImDMA2)]^{2+}$	1.9359(2)	1.9608(2)	2.1056(2)	1.9511(2)	_	1.830(2)
$[Co(PY5ImDMA2)]^{3+}$	1.923(5)	1.960(5)	1.930(6)	1.974(5)	1.950(5)	1.853(7)

sensitized solar cells were measured for each electrolyte condition, and the average is given with standard deviations.

■ RESULTS AND DISCUSSION

The hexadentate ligands PY5ImBr, PY5ImDMA1Br, and PY5ImDMA2Br were synthesized in three steps (Figure 2). First, one-pot syntheses of PY3FDMA1 and PY3FDMA2 were developed which took inspiration from the previously reported synthesis of PY3F. 30 By introducing dimethyl amine groups in the para positions of the pyridine precursors, the tris(pyridyl) unit could have three variations in donating ability. The three pyridine units were coupled together by addition of lithiated ethyl pyridine to the appropriate 2-fluoropyridine derivative, followed by the addition of the appropriate 2,6-difluoropyridine derivatives. The second step was the nucleophilic substitution of fluorine with imidazole following a previously developed synthesis method for similar multidentate ligands to introduce the NHC unit.³¹ In a similar method to the synthesis of PY4Im, the resulting compounds PY3Im, PY3ImDMA1, and PY3ImDMA2 were then reacted with bromobis(2-pyridyl)methane to give the cationic hexadentate ligand products in good yields (61-78%).²³

Transmetallation with Ag₂O was attempted to coordinate the PY5Im ligand to cobalt metal centers following the procedure reported for the analogous PY4Im ligand. While coordination to the silver ion was found to occur, coordination attempts to Co(OTf)₂ with the silver-bound ligand resulted in mixtures of Co(II) and Co(III) ligand-bound complexes along with other impurities. We therefore attempted deprotonation with an excess of K2CO3 as a mild base which resulted in successful coordination to the Co(II) center with the carbene and pyridine units without partial oxidation to Co(III). The bromide ion was removed with thallium(I) triflate resulting in the Co(II) complexes: [Co(PY5Im)](OTf)2, [Co-(PY5ImDMA1)](OTf)₂, and [Co(PY5ImDMA2)](OTf)₂ (Figure 3). The Co(II) complexes were then oxidized in the presence of ferrocenium triflate to result in the Co(III) complexes [Co(PY5Im)](OTf)₃, [Co(PY5ImDMA1)](OTf)₃, and [Co(PY5ImDMA2)](OTf)₃.

Crystals of 10a, 10b, 11a, 11b, 12a, and 12b were grown and analyzed via single-crystal X-ray diffraction. Interestingly, the structures showed that all three Co(II) complexes were five-coordinate, while the Co(III) complexes were six-coordinate, despite the ligand being hexadentate (Figure 4 and Table 1). For the [Co(PYSIm)](OTf)₂ complex, two different structures (A and B) were present within the unit cell. The A and B structures were found to be nearly identical, so only the A structure is shown in this work (Figure 3 and Table 1). The change in the coordination number due to the redox event has molecular switch behavior; however, other cobalt Co(III/II) molecular switches generally change stereochemistry and not the coordination number. 32-34 Each Co(II) complex has a pseudo square pyramidal geometry but with

large distortions from the ideal geometry. The geometry is likely due to strong Jahn—Teller distortion from the low-spin d7 electronic configuration of all the Co(II) complexes, as confirmed by the Evan's method (Figure 5 and Table 2). Large

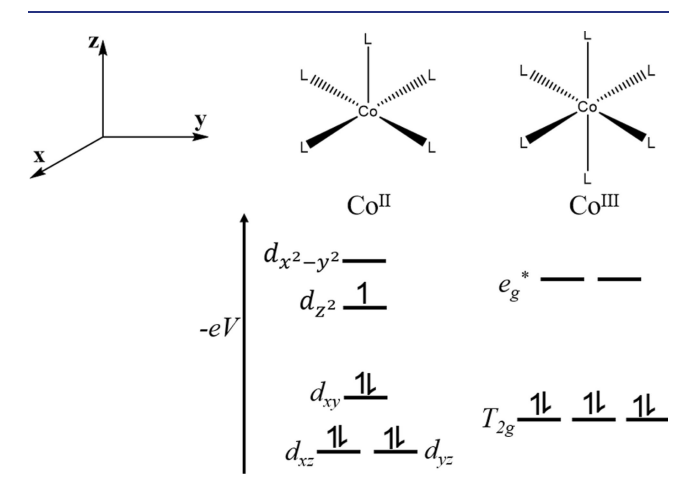


Figure 5. Effects of Jahn—Teller distortion on crystal field splitting of Co(II) and Co(III) complexes reported.

distortions from octahedral geometries have also been seen for the [Co(PY5Me₂) (CN)](OTf), [Co(PY5Me₂DMP-CN)]- $(PF_6)_2$, and $[Co(ttcn)](BF_4)_2$ complexes; however, these examples are all six-coordinate. 20,21,35 There are other examples of both five-coordinate and six-coordinate low-spin Co(II) complexes, and a cursory observation is that the ligand systems with more flexibility are typically six-coordinate due to their ability to accommodate the Jahn-Teller distortion. 36-39 One example utilizing a pentadentate thiocarbohydrazidebased ligand with four low-spin Co(II) metal centers demonstrates two six-coordinate metal centers and two fivecoordinate metal centers. 40 However, the same ligand coordinated to four Fe(III) metal centers is octahedral. In both complexes, the bond angles of the coordinating atoms with the metal are distorted, indicating significant strain. Likely, in the case of low-spin Co(II) complexes, the energy difference between an octahedral and square pyramidal geometry is close enough that ligand strain is more of a contributing factor than in the case of the octahedral Fe(III) cluster. The Co(II) to ligand bond distances and angles are nearly identical for all the complexes measured, indicating that the DMA additions have little impact. Upon oxidation, each complex coordinates the pendant pyridine moiety to form a distorted octahedral geometry. The three Co(III) complexes have nearly identical coordination environments, indicating that the reorganization energies should be very similar for all three Co(III/II) couples.

Cyclic voltammograms were collected for each complex in acetonitrile (Figure 6). The Co(III/II) and Co(III/I) waves

Table 2. Effective Magnetic Moment, Redox Potential vs Fc⁺/Fc, Diffusion Coefficient, and Electron Self-Exchange Rate Constants for Co(II/III) Redox Couples

Co(II) complex	$\mu_{ m eff}~(\mu_{ m b})$	$E_{1/2}\nu s Fc^+/Fc$ (V)	$D \left(\text{cm}^2 \text{ s}^{-1} \right)$	$k_{11} \ (M^{-1} \ s^{-1})$
$[Co(bpy)_3](PF_6)_2$	4.6 51	-0.066	$8.7 \pm 0.4 \times 10^{-652}$	0.27 19
$[Co(PY5Im)](OTf)_2$	1.81 ± 0.02	-0.205 ± 0.003	$6.6 \pm 0.5 \times 10^{-6}$	4.2 ± 0.3
$[Co(PY5ImDMA1)](OTf)_2$	2.02 ± 0.06	-0.299 ± 0.003	$8.2 \pm 0.9 \times 10^{-6}$	2.4 ± 0.1
$[Co(PY5ImDMA2)](OTf)_2$	1.72 ± 0.05	-0.426 ± 0.001	$9.7 \pm 0.8 \times 10^{-6}$	2.2 ± 0.1

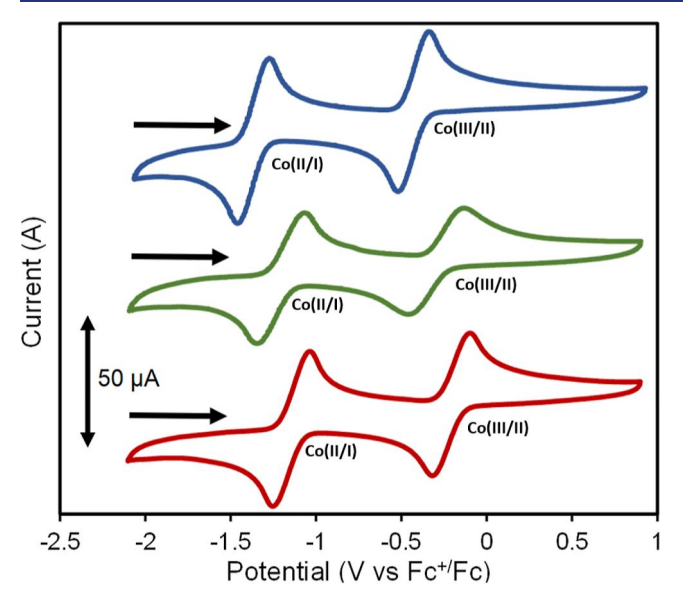


Figure 6. Cyclic voltammograms of 2 mM $[Co(PY5Im)](OTf)_2$ (red), $[Co(PY5ImDMA1)](OTf)_2$ (green), and $[Co-(PY5ImDMA2)](OTf)_2$ (blue) in 0.1 M LiOTf in acetonitrile at a scan rate of 100 mV s⁻¹. The initial scan direction is indicated with an arrow, and each cyclic voltammogram was started at approximately $-2.1 \text{ V vs Fc}^+/Fc$.

were visible, with anodic and cathodic peak currents linear with scan rate and a ratio close to 1, thus assigned to be electrochemically quasi-reversible (Figures S4-S9). We note that a four-coordinate Co(III) complex has been reported with similar behavior. 41 In both the reported complex and these complexes, the change in coordination results in a rearrangement in the ligand environment around the metal but with no new ligands in the inner coordination sphere. The change in the coordination number will affect the inner-sphere reorganization energy, but it seems to not affect the electrochemical (quasi-) reversibility in both cases. This is analogous to complexes that undergo large metal-to-ligand bond distance changes upon electron transfer without a change in the coordination number. The diffusion coefficients for the $[Co(PYSIm)](OTf)_{3/2}$, $[Co(PYSImDMA1)](OTf)_{3/2}$, and $[Co(PY5ImDMA2)](OTf)_{3/2}$ complexes were found to be nearly identical to each other and to [Co(bpy)₃](PF₆)_{3/2} (Table 2). Introduction of the NHC carbene unit into the ligand framework results in a 140 mV negative shift in the redox potential of [Co(PY5Im)](OTf)_{3/2} compared to that of $[Co(bpy)_3]^{3+/2+}$. The redox potential of the unsubstituted [Co(PY5Im)](OTf)_{3/2} couple was also found to be approximately 10 mV negative of the [Co(PY4Im) (ACN)](OTF)_{3/2} couple and several hundred millivolts negative of the [Co(PY5Me₂)(ACN)]_{3/2} couple previously reported.^{23,42} The addition of the electron-donating dimethyl amine groups to the ligand results in additional shifts in the redox potential of approximately 100 mV for each dimethyl amine group

relative to the parent complex $[Co(PY5Im)]^{3+/2+}$. Similar shifts in redox potential have been previously reported with terpyridine ligands on cobalt with varying numbers of dimethyl amine groups. ⁴³

Stopped-flow experiments were performed to determine the electron-transfer self-exchange rate constant for each cobalt complex by monitoring cross-exchange reactions. The ferrocene derivatives FcMe2, FcMe8, and FcMe10 were used as standards due to their well-defined self-exchange rate constants and their close redox potentials to the cobalt complexes to slow down the observed cross-exchange rates to the instrument's time scale. The self-exchange rate constant of each ferrocene derivative was measured by the NMR line broadening method in deuterated acetonitrile with LiOTf supporting electrolyte to imitate conditions in DSSC electrolytes (Tables S10–S12).⁴⁴ The self-exchange rate constants were found to be $6.8 \pm 0.8 \times 10^6$, $2.0 \pm 0.4 \times 10^7$, and $3.8 \pm 0.8 \times 10^6$, $2.0 \pm 0.4 \times 10^7$, and $2.8 \pm 0.8 \times 10^6$, $2.0 \pm 0.4 \times 10^7$, and $2.8 \pm 0.8 \times 10^6$, $2.0 \pm 0.4 \times 10^7$, and $2.8 \pm 0.8 \times 10^6$. $0.7 \times 10^7 \,\mathrm{M}^{-1} \,\mathrm{s}^{-1}$ for $[\mathrm{FcMe_2}](\mathrm{OTf})_{1/0}$, $[\mathrm{FcMe_8}](\mathrm{OTf})_{1/0}$, and $[FcMe_{10}](OTf)_{1/0}$, respectively, all of which are in good agreement with previous reports.^{45,46} Knowing the selfexchange rate constant and redox potential of each ferrocene derivative, cross-exchange experiments were performed to determine the electron-self-exchange rate constant of each cobalt complex (eqs 1-3). Pseudo-first-order conditions were utilized where the ferrocene complexes were prepared at a 10fold excess or greater relative to the cobalt complexes. The concentration of one of the ferrocene derivatives was then increased to change the observed rate constant of the reaction. The data were fit to a single exponential function to extract the observed rate constant for each concentration (eq 4)

$$[Co(PYSIm)](OTf)_2 + [FcMe_2](OTf)$$

$$\xrightarrow{k_{12}} [Co(PYSIm)](OTf)_3 + [FcMe_2]$$
(1)

 $[Co(PY5ImDMA1)](OTf)_3 + [FcMe_8]$

$$\xrightarrow{k_{12}} [Co(PY5ImDMA1)](OTf)_2 + [FcMe_8](OTf)$$
(2)

 $[Co(PY5ImDMA2)](OTf)_3 + [FcMe_{10}]$

$$\xrightarrow{k_{12}} [Co(PYSImDMA2)](OTf)_2 + [FcMe_{10}](OTf)$$
(3)

$$A = A_{\infty} + (A_0 - A_{\infty})e^{-k_{\text{obs}}t}$$
 (4)

For each Co(II) complex, a metal-to-ligand charge-transfer absorbance feature is seen at the edge of the visible spectrum, providing a strong signal to observe at 400 nm for the experiments (Figures S1–S3). In the case of [Co(PY5Im)]-(OTf)_{3/2}, the [Co(PY5Im)](OTf)₂ complex was oxidized by [FcMe₂](OTf) resulting in a decrease in the signal at 400 nm, as shown in Figure 7a. Fitting each exponential, $k_{\rm obs}$, was obtained for each [FcMe₂](OTf) concentration. From the

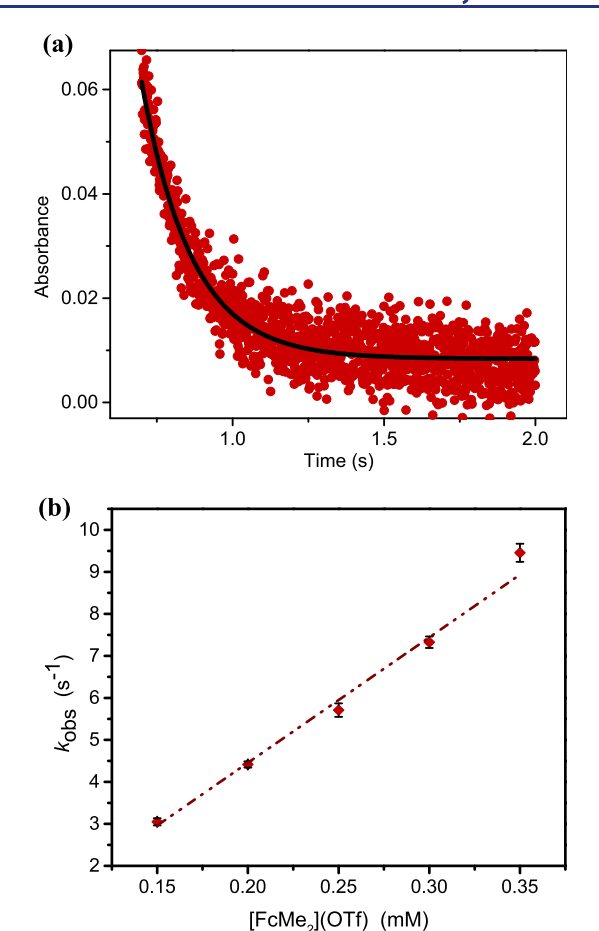


Figure 7. (a) Cross-exchange reaction between 0.015 mM [Co-(PYSIm)](OTf)₂ with 0.25 mM [FcMe₂](OTf) observing the decay of the $[Co(PYSIm)](OTf)_2$ signal at 400 nm. (b) Pseudo-first-order rate constants, k_{obs} , vs the concentration of $[FcMe_2](OTf)$ for the reactions between $[Co(PYSIm)](OTf)_2$ and $[FcMe_2](OTf)$.

slope of $k_{\rm obs}$ versus concentration of [FcMe₂](OTf), the cross-exchange rate constant k_{12} was obtained (Figure 7b). Using the equilibrium constant K_{12} , determined from the difference in redox potentials and the measured self-exchange rate constant of the [FcMe₂](OTf)_{1/0}, the electron self-exchange rate constant k_{11} was determined from the simplified Marcus cross-relation for the [Co(PY5Im)](OTf)_{3/2} couple (Table 2 and Table S13).

$$k_{12} = \sqrt{k_{11}k_{22}K_{12}} \tag{5}$$

For $[Co(PYSIm)](OTf)_{3/2}$, a self-exchange rate constant of $4.2 \pm 0.3 \ M^{-1} \ s^{-1}$ was found, which is surprisingly small. $[Co(PYSImDMA1)](OTf)_{3/2}$ and $[Co(PYSImDMA2)]-(OTf)_{3/2}$ were also crossed with $[FcMe_8](OTf)_{1/0}$ and $[FcMe_{10}](OTf)_{1/0}$, respectively. The resulting electron self-exchange rate constants of the three redox shuttles fall within close agreement, suggesting that adjustments in potential by the dimethyl amine groups have little to no effect on the reorganization energy $(Table\ 2)$. For comparison, the self-exchange rate constant for the low-spin $[Co(ttcn)_2]^{3+/2+}$ is $9.1 \pm 0.7 \times 10^3 \ M^{-1} \ s^{-1}$. The self-exchange rate constant for the related $[Co(PYSMe_2)\ (CN)]^{2+/+}$ complex was determined to be an intermediate value of $20 \pm 5.5 \ M^{-1} \ s^{-1}$, which was necessarily measured without a supporting electrolyte and therefore represents an underestimated basis of comparison.

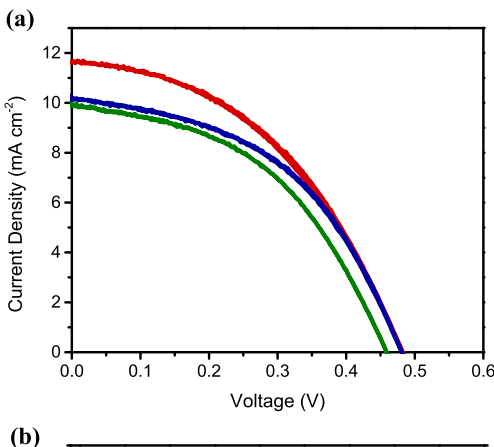
In contrast, $[\text{Co(bpy)}_3](\text{PF}_6)_{3/2}$ has an order of magnitude slower self-exchange rate constant of 0.27 \pm 0.06 M⁻¹ s⁻¹, which was attributed to a large inner sphere reorganization energy from the structural changes associated with low-spin to high-spin Co(III/II) electronic configurations. ¹⁹

Values of λ_i were calculated by subtracting the outersphere reorganization energy, λ_0 , from the total reorganization energy of the self-exchange reaction, $\lambda_{\rm se}$, following the procedure previously reported.⁴⁹ Details of the calculations and results are provided in the Supporting Information (Table S14). The λ_i of the $[Co(PY5Im)](OTf)_{3/2}$ couple is ~0.37 eV lower than that of $[Co(bpy)_3](PF_6)_{3/2}$; 2.2 versus 2.6 eV, respectively. The average Co-N and Co-C bond-length change of the five donor moieties of the PY5Im ligand which remain bound to the Co center in both oxidation states is only ca. 0.05 Å. For comparison, an average change of 0.19 Å in Co-N bond lengths from the reduction of the [Co(phen)₃]³⁺ to [Co- $(phen)_3$ ²⁺ complexes, structural analogues to $[Co(bpy)_3]^{3+/2+}$, was determined previously.⁵⁰ Considering the relatively small average bond length changes for [Co(PY5Im)](OTf)_{3/2}, we can deduce the reversible binding of an exogenous ligand contributes on the order of 2 eV to the total reorganization energy. Thus, while tuning the cobalt complexes toward a lowspin Co(II) species does appear to reduce the inner sphere reorganization energy significantly, as evidenced by the relatively small bond length changes; this is largely offset by the large structural changes resulting from five-coordinate Co(II) to six-coordinate Co(III) molecular switching behavior. This finding opens up an unexpected additional strategy to control electron-transfer kinetics.

Dye-sensitized solar cells employing the standard organic sensitizer LEG4 were prepared to evaluate the performance of the new series of redox shuttles (Figure S38).⁵³ All the Co(II) concentrations were limited to 0.16 M due to solubility limitations of the [Co(PY5ImDMA2)](OTf)₂ complex. We found that the common base additive 4-tert-butylpyridine (TBP) coordinates to the open site of the [Co(PY5Im)]-(OTf)₂ complex. Upon addition of TBP to the electrolyte, as well as other common coordinating bases, the solution potential shifts negative by approximately 200 mV, which complicates analysis and diminishes performance. This shift in solution potential is attributed to coordination of the TBP to the open Co(II) sight, similar to prior reports on Cu(I) complexes.⁵⁴ This observation supports the fact that strain is an important factor for the three PY5Im Co(II) complexes being five-coordinate. Otherwise, the free base in solution would not coordinate readily to the complex, while the hanging pyridine remains uncoordinated. Several alternative bases were investigated and the inductively withdrawn base 4-(trifluoromethyl)pyridine (TFMP) and the sterically hindered based 2,6-di-tert-butylpyridine were found to be compatible with the cobalt complexes, with no significant shifts in solution potential observed (Table S15). Therefore, TFMP was used as a base additive to improve the voltage output of the cells. A comparison of TFMP versus TBP with $[Co(bpy)_3]^{3+/2+}$ is provided in the Supporting Information showing a higher photocurrent and lower photovoltage with TFMP (Table S16 and Figures S43-S46).

The electrolyte of all cells consisted of 0.16 M Co(II), 0.04 M Co(III), 0.1 M Li(OTf), and 0.2 M TFMP. Comparing the current density (*J*) versus the applied voltage (*V*) behavior under simulated AM 1.5 illumination, each redox shuttle produces similar current densities, with the exception of

[Co(PYSIm)]^{3+/2+} being slightly larger (Figure 8a and Table 3). This suggests that dye regeneration is not limiting device



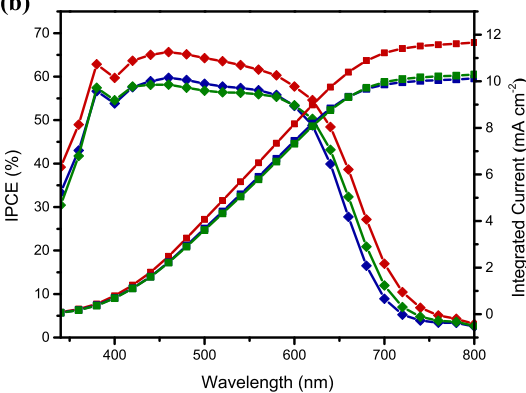


Figure 8. (a) Current density vs voltage curves under 100 mW cm⁻² illumination for $[Co(PYSIm)](OTf)_{3/2}$ (red), $[Co(PYSImDMA1)](OTf)_{3/2}$ (green), and $[Co(PYSImDMA2)](OTf)_{3/2}$ (blue). (b) The incident photon-to-current conversion efficiency (diamonds) of each redox couple and the integrated I_{sc} from the IPCE spectra (squares).

performance since more negative solution potentials of the redox couple would increase the driving force for dye regeneration and photocurrent if this were the case. Inspection of the incident photon-to-current efficiency (IPCE) spectra demonstrates an increase in IPCE response for [Co-(PYSIm)] $^{3+/2+}$ relative to [Co(PYSImDMA1)] $^{3+/2+}$ and [Co-(PYSImDMA2)] $^{3+/2+}$. The integrated current densities found from IPCE align well with those from the $J\!-\!V$ measurements (Figure 8b). This indicates that diffusion of the redox shuttles through the TiO2 is not a major issue since the current density from the AM 1.5 spectrum matches well with the IPCE integrated current density which is measured at a lower light intensity. 55

The IPCE is determined by the product of the lightharvesting efficiency, the electron injection efficiency, the dye regeneration efficiency, and the charge collection efficiency. The light-harvesting efficiency is nominally identical for the three electrolytes because the same dye and photoanode are utilized and minimal differences are present in the competitive absorbance over the 450-650 nm region. The observation that the IPCEs from the three electrolytes are relatively flat over the 450-650 nm region also indicates that they are not controlled by light-harvesting or the charge collection efficiency which would result in shapes resembling the dye absorbance spectrum. 19 Therefore, the higher IPCE of [Co(PY5Im)]^{3+/2+} relative to that of [Co(PY5ImDMA1)]^{3+/2+} and [Co-(PY5ImDMA2)]3+/2+ can be attributed to either a higher regeneration or injection efficiency. Differences in regeneration efficiency are counterintuitive and ruled out above. Therefore, we propose that the electron injection efficiency is higher for [Co(PY5Im)]^{3+/2+}. This is quite unexpected since the dye and electrolyte additives are constant and therefore suggests that the conduction band is shifted negatively for [Co- $(PY5ImDMA1)]^{3+/2+}$ and $[Co(PY5ImDMA2)]^{3+/2+}$ which inhibits injection.

Surprisingly, the $V_{\rm oc}$ of each new cobalt redox shuttle is within error of each other despite over 200 mV difference in the formal solution potential. A more negative solution potential is anticipated to decrease the open-circuit voltage in the absence of competing factors. A constant V_{oc} however, indicates the Fermi level shifts with the solution potential. Decreased recombination will increase the electron concentration in TiO2 at steady state and will result in the Fermi level moving closer to the conduction band edge which may account for some of the shift.⁵⁶ We note, however, that a 200 mV shift in Fermi level would result from 3-4 orders of magnitude reduction in recombination (59 mV/decade), which is much larger than expected. Alternatively, a conduction band edge shift can likewise affect the voltage. This conduction band edge shift agrees with the analysis of the IPCE spectrum above. We have shown previously that the band edges of nanoparticle TiO₂ can vary quite a bit due to charging,⁵⁷ but the band shift due to the addition of DMA groups on the redox couple is very surprising and the exact cause is not clear at this point and is the subject of future investigations.

The electrolyte based on $[Co(PY5Im)]^{3+/2+}$ was selected for further testing with an NIR record photocurrent-generating dye system, AP25 + D35 (Figure S38), 10 based on $[Co(PYSIm)]^{3+/2+}$ exhibiting the highest photocurrent of the series with LEG4-based devices. Devices were fabricated and compared to the $[Co(bpy)_3]^{3+/2+}$ redox shuttle which has a modest regenerative driving force (240 mV) for this redox shuttle with the AP25 + D35 system. $[Co(PY5Im)]^{3+/2+}$ -based devices resulted in a higher short-circuit photocurrent density compared to $[Co(bpy)_3]^{3+/2+}$ -based devices (19.8 mA cm⁻² vs 18.0 mA cm⁻², Table 4 and Figure 9). The larger photocurrent is likely due to faster regeneration from the combination of faster self-exchange kinetics and a larger regenerative driving force (380 mV) for [Co(PY5Im)]^{3+/2+} when compared with [Co(bpy)₃]^{3+/2+}. This change in photocurrent is primarily observed as an increase in the IPCE between 600-850 nm

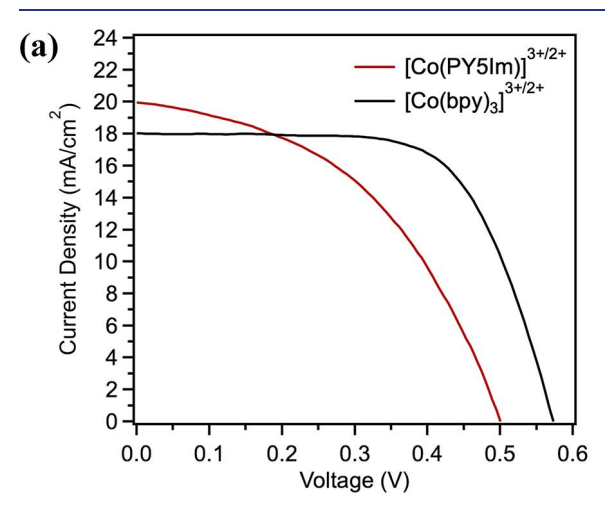
Table 3. DSSC Summarized Performance under 100 mW cm⁻² Illumination

electrolyte	$E_{\rm sol} (V)^a$	$V_{\rm oc}$ (V)	$J_{\rm sc}~({\rm mA~cm}^{-2})$	FF	PCE
$[Co(PY5Im)]^{3+/2+}$	-0.274	0.47 ± 0.02	11.6 ± 0.5	0.42 ± 0.02	2.3 ± 0.2
$[Co(PY5ImDMA1)]^{3+/2+}$	-0.352	0.45 ± 0.02	9.9 ± 0.7	0.42 ± 0.03	1.9 ± 0.2
$[Co(PY5ImDMA2)]^{3+/2+}$	-0.460	0.47 ± 0.01	10.3 ± 0.4	0.45 ± 0.03	2.2 ± 0.2

^aThe solution potential of each electrolyte measured versus Fc⁺/Fc prior to injection into the devices.

Table 4. Device Data for AP25 + D35 Devices with $[Co(PY5Im)]^{3+/2+}$ and $[Co(bpy)_3]^{3+/2+}$

	$V_{ m OC}~({ m mV})$	$J_{\rm SC}~({\rm mA~cm}^{-2})$	FF	PCE
$[Co(PY5Im)]^{3+/2+}$	503 ± 4	19.8 ± 0.4	0.45 ± 0.01	4.48 ± 0.12
$[Co(bpy)_3]^{3+/2+}$	576 ± 3	18.0 ± 0.2	0.65 ± 0.01	6.75 ± 0.09



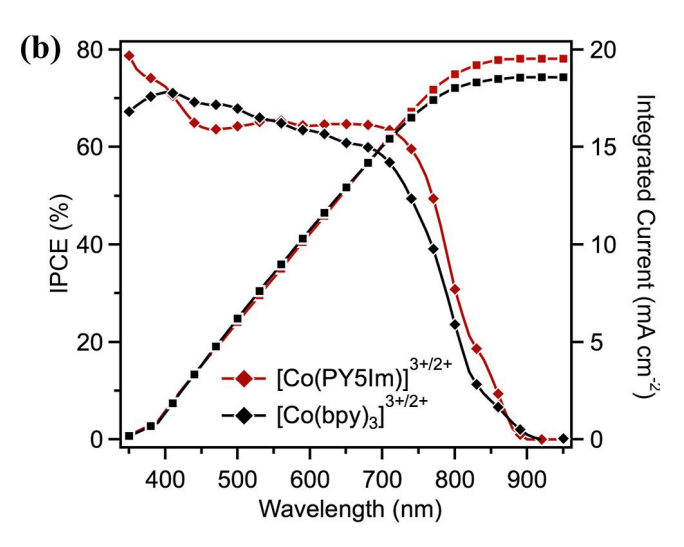


Figure 9. (a) JV plots of **AP25** + **D35**-based DSSC devices with $[Co(PY5Im)]^{3+/2+}$ and $[Co(bpy)_3]^{3+/2+}$. (b) IPCE plots of **AP25** + **D35**-based DSSC devices with $[Co(PY5Im)]^{3+/2+}$ and $[Co(bpy)_3]^{3+/2+}$.

(Figure 7b). The broadening of the spectra indicates increased charge collection efficiency at wavelengths where the dye, AP25, has a lower extinction coefficient and D35 is nonabsorbing. This observation suggests there is decreased recombination for the $[Co(PYSIm)]^{3+/2+}$ redox shuttle.⁵⁵

To better understand recombination losses, small modulated photovoltage transient (SMPVT) studies were carried out to probe the changes in electron lifetime in TiO_2 (Figure 10). A longer lifetime is observed with $[\text{Co}(\text{PYSIm})]^{3+/2+}$ at the V_{OC} of this DSSC device than with $[\text{Co}(\text{bpy})_3]^{3+/2+}$ at the V_{OC} of this DSSC device. However, extrapolating the trend lines to a common voltage value reveals a modestly longer electron lifetime with $[\text{Co}(\text{bpy})_3]^{3+/2+}$ than that with $[\text{Co}(\text{PYSIm})]^{3+/2+}$ at a hypothetical common voltage. Thus, the longer lifetime observed with $[\text{Co}(\text{PYSIm})]^{3+/2+}$ at the respective DSSC device V_{OC} is likely due in part to a lower driving force for recombination between electrons in the TiO₂

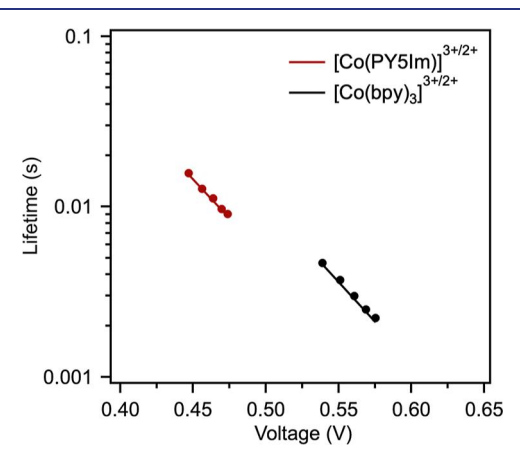


Figure 10. SMPVT plots of **AP25** + **D35**-based DSSC devices with $[Co(PY5Im)]^{3+/2+}$ and $[Co(bpy)_3]^{3+/2+}$.

CB and the redox shuttle. To further analyze the recombination rate, the total $V_{\rm OC}$ loss ($V_{\rm OC}$) values were analyzed via the equation $V_{\rm OC}$ loss = $V_{\rm OC}$ max - $V_{\rm OC}$ obs, where $V_{\rm OC}$ is the $V_{\rm OC}$ observed in the DSC device and $V_{\rm OC}$ is the energetic difference between the TiO₂ CB and the redox shuttle potential. Assuming a commonly taken conduction band value of -0.5 V versus for TiO₂ and a 300 mV TiO₂ CB shift (see discussion below) to a more positive value, a $V_{\rm OC}$ max of 0.63 V is possible with $[{\rm Co(PYSIm)}]^{3+/2+}$ and 1.07 V is possible with $[{\rm Co(bpy)_3}]^{3+/2+}$ which does not show the same TiO₂ CB shift (see discussion below). A $V_{\rm OC}$ loss of 130 mV is observed with $[{\rm Co(PYSIm)}]^{3+/2+}$ compared to a value of 490 mV with $[{\rm Co(bpy)_3}]^{3+/2+}$.

The recombination kinetics can generally be described in terms of Marcus theory, where the rate constant is a function of driving force and reorganization energy. In our previous report on the only other low-spin Co(II) redox shuttle employed in DSSCs, $[Co(ttcn)_2]^{3+/2+}$, the significantly lower reorganization energy resulted in faster recombination, shorter diffusion lengths, and lower photocurrents relative to $[Co(bpy)_3]^{3+/2+}$. In contrast, the modestly lower reorganization energy of $[Co(PY5Im)]^{3+/2+}$ relative to that of $[Co(bpy)_3]^{3+/2+}$ is compensated by a concomitant more negative potential which reduces the driving force for recombination. As a result, $[Co(PY5Im)]^{3+/2+}$ allows superior dye regeneration relative to $[Co(bpy)_3]^{3+/2+}$ without sacrificing recombination losses. Full exploitation of this advantage will require pairing with dyes capable of absorbing further into the NIR, which is currently being pursued in our labs.

Possible relative shifts in the conduction band can be approximated by correlating the electron density in ${\rm TiO_2}$ with the charge density, providing that the same porosity, thickness, and particle sizes are used in DSSC device fabrication. ⁵⁹ In these experiments, the electronic states in ${\rm TiO_2}$ are shifted toward lower energy for ${\rm [Co(PYSIm)]^{3+/2+}}$ relative to ${\rm [Co(bpy)_3]^{3+/2+}}$ at the same concentration of electrons in ${\rm TiO_2}$ to give an approximately 300 mV lower voltage (Figure 11, dashed lines). Since the $V_{\rm OC}$ of the devices is observed to only be about 73 mV lower for the ${\rm [Co(PYSIm)]^{3+/2+}}$ -based

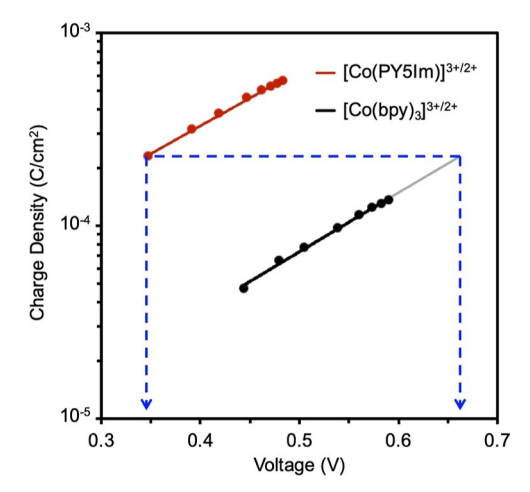


Figure 11. Extracted charge density vs voltage plots of AP25 + D35-based DSSC devices with $[Co(PY5Im)]^{3+/2+}$ and $[Co(bpy)_3]^{3+/2+}$. Note: the $[Co(bpy)_3]^{3+/2+}$ trendline is forecasted in gray beyond the data points available to allow for a common charge density assessment of the two data sets.

DSSC devices relative to $[\text{Co(bpy)}_3]^{3+/2+}$, the additional 227 mV change in voltage observed from the charge extraction measurement at open circuit suggests a shift of this amount in the TiO_2 CB energy to lower values for $[\text{Co(PYSIm)}]^{3+/2+}$ relative to $[\text{Co(bpy)}_3]^{3+/2+}$, without device $V_{\text{OC}}^{\text{loss}}$. This indicates that the $V_{\text{OC}}^{\text{loss}}$ is significantly less for $[\text{Co(PYSIm)}]^{3+/2+}$ since the $V_{\text{OC}}^{\text{max}}$ term is determined by the TiO_2 CB energy. Thus, the $V_{\text{OC}}^{\text{loss}}$ with $[\text{Co(PYSIm)}]^{3+/2+}$ would be approximately 130 mV which compares favorably to the 490 mV loss with $[\text{Co(bpy)}_3]^{3+/2+}$. We note that a 130 mV $V_{\text{OC}}^{\text{loss}}$ is exceptional within the DSSC field.

CONCLUSIONS

A new hexadentate ligand and redox system have been prepared that have resulted in three new Co(III/II) redox shuttles. The carbene and addition of dimethyl amine groups result in a tunable framework at significantly negative redox potentials. Introduction of the strong-field NHC carbene induced low-spin Co(II) complexes which increased the electron self-exchange rate constant. The self-exchange rate was modestly improved relative to other low-spin Co(II) redox couples measured previously due to the five-coordinate to sixcoordinate molecular switch behavior. The driving force for dye regeneration could likely be minimized further if the distortions of low-spin Co(II) redox shuttles were reduced to increase the self-exchange rate. Unfortunately, the Co(II) complexes suffered from undesirable coordination effects in the presence of more donating pyridine bases that prevented further increase of the open-circuit voltage by adding them to the electrolyte. The lower self-exchange and instability to bases could possibly be fixed by a more flexible strong-field ligand system such as ttcn that can better absorb the structural distortions. The redox shuttle series had high photocurrents with the LEG4 sensitizer, were not limited by dye regeneration, and appeared well suited for NIR dye systems with more negative HOMO energy levels like that of the AP25 + D35 system tested here. The [Co(PY5Im)]^{3+/2+} redox shuttle improved the photocurrent relative to $[Co(bpy)_3]^{3+/2+}$ with AP25 + D35, providing a proof of concept of more negative redox shuttles paired with NIR sensitizers giving improved photocurrent. Future work points toward integrating this redox series with dyes that absorb further into the NIR which would enable single devices or tandem DSSCs that could harvest photons from 300–1200 nm analogous to silicon photovoltaics.

ASSOCIATED CONTENT

Supporting Information

The Supporting Information is available free of charge at https://pubs.acs.org/doi/10.1021/jacs.2c12017.

Details of synthetic methods and characterization of all ligands and complexes reported herein, discussion of magnetic moment and self-exchange and reorganization energy calculations, and electrochemical impedance measurements (PDF)

Accession Codes

CCDC 2045984, 2059073, 2064744, 2074904, 2075461, and 2080559 contain the supplementary crystallographic data for this paper. These data can be obtained free of charge via www.ccdc.cam.ac.uk/data_request/cif, or by emailing data_request@ccdc.cam.ac.uk, or by contacting The Cambridge Crystallographic Data Centre, 12 Union Road, Cambridge CB2 1EZ, UK; fax: +44 1223 336033.

AUTHOR INFORMATION

Corresponding Authors

Jared H. Delcamp – UES, Inc. Research Scientist, Air Force Research Labs, Materials and Manufacturing Directorate, WPAFB, Ohio 45433-7817, United States; oorcid.org/ 0000-0001-5313-4078; Email: jdelcamp@ues.com

Thomas W. Hamann — Department of Chemistry, Michigan State University, East Lansing, Michigan 48823, United States; orcid.org/0000-0001-6917-7494; Email: hamann@chemistry.msu.edu

Authors

Austin L. Raithel — Department of Chemistry, Michigan State University, East Lansing, Michigan 48823, United States William E. Meador — Department of Chemistry and Biochemistry, Coulter Hall, University of Mississippi, University, Mississippi 38677, United States; ● orcid.org/0000-0002-9869-026X

Tea-Yon Kim — Department of Chemistry, Michigan State University, East Lansing, Michigan 48823, United States Richard J. Staples — Department of Chemistry, Michigan State University, East Lansing, Michigan 48823, United States; orcid.org/0000-0003-2760-769X

Complete contact information is available at: https://pubs.acs.org/10.1021/jacs.2c12017

Notes

The authors declare no competing financial interest.

ACKNOWLEDGMENTS

We thank the Chemical Sciences, Geosciences, and Biosciences Division, Office of Basic Energy Sciences, Office of Science, the U.S. Department of Energy grant no. DE-SC0017342 for their generous support of this work. NSF grant 1954922 is thanked for supporting the NIR studies. This material is based upon work supported by the National Science Foundation Graduate Research Fellowship Program awarded to WEM. Any opinions, findings, and conclusions or recommendations expressed in this material are those of the

author(s) and do not necessarily reflect the views of the National Science Foundation. The Rigaku Synergy S Diffractometer was purchased with Support from the MRI program by the National Science Foundation under grant no. 1919565 for use at the Center for Crystallographic Research, MSU. This paper is adapted from A.L.R.'s PhD thesis.

■ REFERENCES

- (1) Hagfeldt, A.; Boschloo, G.; Sun, L.; Kloo, L.; Pettersson, H. Dye-Sensitized Solar Cells. *Chem. Rev.* **2010**, *110*, 6595–6663.
- (2) Muñoz-García, A.; Benesperi, I.; Boschloo, G.; Concepcion, J. J.; Delcamp, J. H.; Gibson, E. A.; Meyer, G. J.; Pavone, M.; Pettersson, H.; Hagfeldt, A.; et al. Dye-Sensitized Solar Cells Strike Back. *Chem. Soc. Rev.* **2021**, *50*, 12450–12550.
- (3) Kakiage, K.; Aoyama, Y.; Yano, T.; Oya, K.; Fujisawa, J.; Hanaya, M. Highly-Efficient Dye-Sensitized Solar Cells with Collaborative Sensitization by Silyl-Anchor and Carboxy-Anchor Dyes. *Chem. Commun.* **2015**, *51*, 15894–15897.
- (4) Mathew, R.; Yella, U.; Gao, M. K.; Humphry-Baker, A.; Curchod, N.; Ashari-Astani, M.; Tavernelli, I.; Rothlisberger, P.; Nazeeruddin, S.; Grätzel, B. F. E. Dye-Sensitized Solar Cells with 13% Efficiency Achieved through the Molecular Engineering of Porphyrin Sensitizers. *Nat. Chem.* **2014**, *6*, 242–247.
- (5) Cao, Y.; Liu, Y.; Zakeeruddin, M.; Hagfeldt, A.; Grätzel, M. Direct Contact of Selective Charge Extraction Layers Enables High-Efficiency Molecular Photovoltaics. *Joule* **2018**, *2*, 1108–1117.
- (6) Zhang, L.; Yang, X.; Wang, W.; Gurzadyan, G. G.; Li, J.; Li, X.; An, J.; Yu, Z.; Wang, H.; Cai, B.; et al. 13.6% Efficient Organic Dye-Sensitized Solar Cells by Minimizing Energy Losses of the Excited State. *ACS Energy Lett.* **2019**, *4*, 943–951.
- (7) Zhang, D.; Stojanovic, M.; Ren, Y.; Cao, Y.; Eickemeyer, F. T.; Socie, E.; Vlachopoulos, N.; Moser, J.; Zakeeruddin, S. M.; Hagfeldt, A.; et al. A Molecular Photosensitizer Achieves a Voc of 1.24 V Enabling Highly Efficient and Stable Dye-Sensitized Solar Cells with Copper(II/I)-Based Electrolyte. *Nat. Commun.* **2021**, *12*, 1777.
- (8) Nazeeruddin, M. K.; Péchy, P.; Renouard, T.; Zakeeruddin, S. M.; Humphry-Baker, R.; Comte, P.; Liska, P.; Cevey, L.; Costa, E.; Shklover, V.; et al. Engineering of Efficient Panchromatic Sensitizers for Nanocrystalline TiO2-Based Solar Cells. *J. Am. Chem. Soc.* **2001**, 123, 1613–1624.
- (9) Kinoshita, T.; Fujisawa, J.; Nakazaki, J.; Uchida, S.; Kubo, T.; Segawa, H. Enhancement of Near-IR Photoelectric Conversion in Dye-Sensitized Solar Cells Using an Osmium Sensitizer with Strong Spin-Forbidden Transition. *J. Phys. Chem. Lett.* **2012**, *3*, 394–398.
- (10) Cheema, H.; Watson, J.; Peddapuram, A.; Delcamp, J. H. A 25 MA Cm-2 Dye-Sensitized Solar Cell Based on a near-Infrared-Absorbing Organic Dye and Application of the Device in SSM-DSCs. *Chem. Commun.* **2020**, *56*, 1741–1744.
- (11) Hamann, T. W.; Jensen, R. A.; Martinson, A. B. F.; Van Ryswyk, V.; Hupp, J. T.; Hamann, T. Advancing beyond Current Generation Dye-Sensitized Solar Cells. *Energy Environ. Sci.* **2008**, *1*, 66–78.
- (12) Snaith, B. H. J. Estimating the Maximum Attainable Efficiency in Dye-Sensitized Solar Cells. *Adv. Funct. Mater.* **2010**, *20*, 13–19.
- (13) Cheema, H.; Watson, J.; Delcamp, J. H. Photon Management Strategies in SSM-DSCs: Realization of a >11 % PCE Device with a 2.3 V Output. *Sol. Energy* **2020**, *208*, 747–752.
- (14) Kinoshita, T.; Nonomura, K.; Jeon, N. J.; Giordano, F.; Abate, A.; Uchida, S.; Kubo, T.; Seok, S. I.; Nazeeruddin, M. K.; Hagfeldt, A.; et al. Spectral Splitting Photovoltaics Using Perovskite and Wideband Dye-Sensitized Solar Cells. *Nat. Commun.* **2015**, *6*, 8834.
- (15) Xiong, D.; Chen, W. Recent Progress on Tandem Structured Dye-Sensitized Solar Cells. *Optoelectron* **2012**, *5*, 371–389.
- (16) Ji, J.-M.; Zhou, H.; Eom, Y. K.; Kim, C. H.; Kim, H. K. 14.2% Efficiency Dye-Sensitized Solar Cells by Co-Sensitizing Novel Thieno[3,2- b]Indole-Based Organic Dyes with a Promising Porphyrin Sensitizer. *Adv. Energy Mater.* **2020**, *10*, 2000124.

- (17) Yang, W.; Vlachopoulos, N.; Hao, Y.; Hagfeldt, A.; Boschloo, G. Efficient Dye Regeneration at Low Driving Force Achieved in Triphenylamine Dye LEG4 and TEMPO. *Phys. Chem. Chem. Phys.* **2015**, *17*, 15868–15875.
- (18) Wilkins, R. G.Kinetics and Mechanism of Reactions of Transition Metal Complexes; Wiley, 2002; Vol. 5.
- (19) Xie, Y.; Baillargeon, J.; Hamann, T. W. Kinetics of Regeneration and Recombination Reactions in Dye-Sensitized Solar Cells Employing Cobalt Redox Shuttles. *J. Phys. Chem. C* **2015**, *119*, 28155–28166.
- (20) Raithel, A. L.; Kim, T.; Nielsen, K. C.; Staples, R. J.; Hamann, T. W. Low-Spin Cobalt(II) Redox Shuttle by Isocyanide Coordination. *Sustain. Energy Fuels* **2020**, *4*, 2497–2507.
- (21) Baillargeon, J.; Xie, Y.; Raithel, A. L.; Ghaffari, B.; Staples, R. J.; Hamann, T. W. Spin-Doctoring Cobalt Redox Shuttles for Dye-Sensitized Solar Cells. *Inorg. Chem.* **2018**, *57*, 11633–11645.
- (22) Zadrozny, J. M.; Freedman, D. E.; Jenkins, D. M.; Harris, T. D.; Clérac, R.; Iavarone, A. T.; Mathonière, C.; Long, J. R. Slow Magnetic Relaxation and Charge-Transfer in Cyano-Bridged Coordination Clusters Incorporating [Re(CN)₇]^{3-/4-}. *Inorg. Chem.* **2010**, 49, 8886–8896.
- (23) Smith, J. M.; Long, J. R. First-Row Transition Metal Complexes of the Strongly Donating Pentadentate Ligand PY4Im. *Inorg. Chem.* **2010**, *49*, 11223–11230.
- (24) Kashif, M. K.; Nippe, M.; Duffy, N. W.; Forsyth, C. M.; Chang, C. J.; Long, J. R.; Spiccia, L.; Bach, U. Stable Dye-Sensitized Solar Cell Electrolytes Based on Cobalt(Ii)/(Iii) Complexes of a Hexadentate Pyridyl Ligand. *Angew. Chem. Int. Ed.* **2013**, *52*, 5527–5531.
- (25) Schlosser, M.; Bobbio, C.; Rausis, T. Regiochemical Flexible Substitutions of Di-, Tri-, and Tetrahalopyridines: The Trialkylsilyl Trick. *J. Org. Chem.* **2005**, *70*, 2494–2502.
- (26) Dyker, G.; Muth, O. Synthesis of Methylene- and Methine-Bridged Oligopyridines. Eur. J. Org. Chem. 2004, 2004, 4319–4322.
- (27) Vedernikov, A. N.; Fettinger, J. C.; Mohr, F. Synthesis and Reactivity of Dimethyl Platinum(IV) Hydrides in Water. *J. Am. Chem. Soc.* **2004**, *126*, 11160–11161.
- (28) Tanabe, Y.; Nakajima, K.; Nishibayashi, Y. Phosphine Oxidation with Water and Ferrocenium(III) Cation Induced by Visible-Light Irradiation. *Chem.—Eur J.* **2018**, 24, 18618–18622.
- (29) Curiac, C.; Hunt, L. A.; Sabuj, A.; Li, Q.; Baumann, A.; Cheema, H.; Zhang, Y.; Rai, N.; Hammer, N. I.; Delcamp, J. H. Probing Interfacial Halogen-Bonding Effects with Halogenated Organic Dyes and a Lewis Base-Decorated Transition Metal-Based Redox Shuttle at a Metal Oxide Interface in Dye-Sensitized Solar Cells. J. Phys. Chem. C 2021, 125, 17647—17659.
- (30) Ünal, E. A.; Wiedemann, D.; Seiffert, J.; Boyd, J. P.; Grohmann, A. Efficient Synthesis of Pentakis- and Tris(Pyridine) Ligands. *Tetrahedron Lett.* **2012**, *53*, 54–55.
- (31) Raba, A.; Anneser, M. R.; Jantke, D.; Cokoja, M.; Herrmann, W. A.; Kühn, F. E. Facile and Scalable Preparation of 2-Imidazolylpyridines. *Tetrahedron Lett.* **2013**, *54*, 3384–3387.
- (32) Bakkar, A.; Cobo, S.; Lafolet, D.; Roldan, E.; Saint-Aman, G.; Royal, G. A Redox- and Photo-Responsive Quadri-State Switch Based on Dimethyldihydropyrene-Appended Cobalt Complexes. *J. Mater. Chem. C* **2016**, *4*, 1139–1143.
- (33) Wan, S.; Li, M.; Zhang, Z.; Xi, H.; Yang, H.; Luo, Q.; Zhu, W.-H. Reversible Light-Driven Magnetic Switching of Salen Cobalt Complex. *Sci. China Chem.* **2020**, *63*, 1191–1197.
- (34) Starikova, A. A.; Chegerev, M. G.; Starikov, A. G. Computational Insight into Magnetic Behaviour of Cobalt Tris(2-Pyridylmethyl)Amine Complexes with Dioxolenes Incorporating Stable Radicals. *Chem. Phys. Lett.* **2021**, *762*, 138128.
- (35) Setzer, W. N.; Ogle, C. A.; Wilson, G. S.; Glass, R. S. 1,4,7-Trithiacyclononane, a Novel Tridentate Thioether Ligand, and the Structures of Its Nickel(II), Cobalt(II), and Copper(II) Complexes. *Inorg. Chem.* 1983, 22, 266–271.
- (36) Drew, M.; McCann, M.; Nelson, S. The Crystal Structures of Iron(II) and Cobalt(II) Complexes of a 30-Membered Macrocyclic Ligand: Observation of Jahn-Teller Distortion in a Six-Coordinate Low-Spin Cobalt(II) Complex. *Inorg. Chim. Acta* 1980, 41, 213–219.

- (37) Jones, R. D.; Summerville, D. A.; Basolo, F. Synthetic Oxygen Carriers Related to Biological Systems. *Chem. Rev.* **1979**, 79, 139–179.
- (38) Caste, M. L.; Cairns, C. J.; Church, J.; Lin, W.; Gallucci, J. C.; Busch, D. H. Cobalt(II) Complex of Produced by a Novel Pentadentate Half-Clathro Half-Cyclidene Ligand a Base-Catalyzed Ligand Rearrangment. *Inorg. Chem.* 1987, 26, 78–83.
- (39) Singh, A. K.; Mukherjee, R. Cobalt(II) and Cobalt (II) Complexes of Thioether-Containing Hexadentate Pyrazine Amide Ligands: C–S Bond Cleavage and Cyclometallation Reaction. *Dalton Trans.* 2008, 260–270.
- (40) Shuvaev, K. V.; Dawe, L. N.; Thompson, L. K. Formation of Unusual Molecular Rectangles and Squares Containing Low Spin and High Spin Co(II) and Fe(II) Centers. *Dalton Trans.* **2010**, *39*, 4768–4776.
- (41) Piskunov, A. S.; Pashanova, K. I.; Bogomyakov, A. V.; Smolyaninov, I. V.; Starikov, G.; Fukin, G. K. Cobalt Complexes with Hemilabile O-Iminobenzoquinonate Ligands: A Novel Example of Redox-Induced Electron Transfer. *Dalton Trans.* **2018**, *47*, 15049–15060.
- (42) Kashif, M. K.; Axelson, J. C.; Duffy, N. W.; Forsyth, C. M.; Chang, C. J.; Long, J. R.; Spiccia, L.; Bach, U. A New Direction in Dye-Sensitized Solar Cells Redox Mediator Development: In Situ Fine-Tuning of the Cobalt(II)/(III) Redox Potential through Lewis Base Interactions. *J. Am. Chem. Soc.* **2012**, *134*, 16646–16653.
- (43) Aroua, S.; Todorova, T. K.; Hommes, P.; Chamoreau, L.; Reissig, H.; Mougel, V.; Fontecave, M. Synthesis, Characterization, and DFT Analysis of Bis-Terpyridyl-Based Molecular Cobalt Complexes. *Inorg. Chem.* **2017**, *56*, 5930–5940.
- (44) Jameson, D. L.; Anand, R. Examination of Electron Transfer Self-Exchange Rates Using NMR Line-Broadening Techniques An Advanced Physical Inorganic Laboratory Experiment. *J. Chem. Educ.* **2000**, 77, 88–89.
- (45) Yang, E. S.; Chan, M.; Wahl, A. C. Electron Exchange between Ferrocene and Ferrocenium Ion. Effects of Solvent and of Ring Substitution on the Rate. *J. Phys. Chem.* **1980**, *84*, 3094–3099.
- (46) Ibrahimova, N. Z.; Jafarove, G. M.; Jafarov, D. B.; Taghiyev, I. U.; Lyatifov, I. U. Research into Kinetics of Electron Exchange Reactions in the System Sym. Octamethylferrocene/Sym. Octamethylferricinium Hexafluorophosphate. *Chem. Probl.* **2019**, *17*, 310–315.
- (47) Marcus, R. A.; Sutin, N. Electron Transfers in Chemistry and Biology. *Biochim. Biophys. Acta* 1985, 811, 265-322.
- (48) Sutin, N.Theory of Electron Transfer Reactions: Insights and Hindsights, Wiley, 1983; Vol. 30.
- (49) Hamann, T. W.; Gstrein, F.; Brunschwig, B. S.; Lewis, N. S. Measurement of the Dependence of Interfacial Charge-Transfer Rate Constants on the Reorganization Energy of Redox Species at n-ZnO/H2O Interfaces. *J. Am. Chem. Soc.* **2005**, *127*, 13949–13954.
- (50) Brunschwig, B.; Creutz, C.; Macartney, D.; Sham, T.-K.; Sutin, N. The Role of Inner-Sphere Configuration Changes in Electron-Exchange Reactions of Metal Complexes. *Faraday Discuss. Chem. Soc.* **1982**, *74*, 113–127.
- (51) Tiwary, S. K.; Vasudevan, S. Spin Crossover in the Ship-in-a-Bottle Compound: Cobalt(II) Tris(Bipyridyl) Encapsulated in Zeolite-Y. Chem. Phys. Lett. 1997, 277, 84—88.
- (52) Katayama, Y.; Nakayama, S.; Tachikawa, N.; Yoshii, K. Electrochemical Behavior of Tris(2,2'-Bipyridine)Cobalt Complex in Some Ionic Liquids. *J. Electrochem. Soc.* **2017**, *164*, H5286–H5291.
- (53) Gabrielsson, E.; Ellis, H.; Feldt, S.; Tian, H.; Boschloo, G.; Hagfeldt, A.; Sun, L. Convergent/Divergent Synthesis of a Linker-Varied Series of Dyes for Dye-Sensitized Solar Cells Based on the D35 Donor. *Adv. Energy Mater.* **2013**, *3*, 1647–1656.
- (54) Wang, Y.; Hamann, T. W. Improved Performance Induced by in Situ Ligand Exchange Reactions of Copper Bipyridyl Redox Couples in Dye-Sensitized Solar Cells. *Chem. Commun.* **2018**, *54*, 12361–12364.

- (55) Klahr, B. M.; Hamann, T. W. Performance Enhancement and Limitations of Cobalt Bipyridyl Redox Shuttles in Dye-Sensitized Solar Cells. *J. Phys. Chem. C* **2009**, *113*, 14040–14045.
- (56) Hamann, T. W.; Ondersma, J. W. Dye-Sensitized Solar Cellredox Shuttles. *Energy Environ. Sci.* **2011**, *4*, 370–381.
- (57) Mandal, D.; Hamann, T. W. Charge Distribution in Nanostructured TiO2 Photoanode Determined by Quantitative Analysis of the Band Edge Unpinning. ACS Appl. Mater. Interfaces 2016, 8, 419–424.
- (58) Zhang, W.; Wu, Y.; Bahng, H. W.; Cao, Y.; Yi, C.; Saygili, Y.; Luo, J.; Liu, Y.; Kavan, L.; Moser, J.; et al. Comprehensive Control of Voltage Loss Enables 11.7% Efficient Solid-State Dye-Sensitized Solar Cells. Energy Environ. Sci. 2018, 11, 1779—1787.
- (59) Boschloo, G.; Häggman, L.; Hagfeldt, A. Quantification of the Effect of 4-Tert-Butylpyridine Addition to I-/I3- Redox Electrolytes in Dye-Sensitized Nanostructured TiO2 Solar Cells. *J. Phys. Chem. B* **2006**, *110*, 13144–13150.
- (60) Baumann, A.; Curiac, C.; Delcamp, J. H. The Hagfeldt Donor and Use of Next-Generation Bulky Donor Designs in Dye-Sensitized Solar Cells. *ChemSusChem* **2020**, *13*, 2503–2512.

□ Recommended by ACS

Lateral Electron and Hole Hopping between Dyes on Mesoporous ZrO₂: Unexpected Influence of Solvents with a Low Dielectric Constant

Sina Wrede, Haining Tian, et al.

MAY 01, 2023

JOURNAL OF THE AMERICAN CHEMICAL SOCIETY

READ **C**

Amine Groups in the Second Sphere of Iron Porphyrins Allow for Higher and Selective 4e-/4H+ Oxygen Reduction Rates at Lower Overpotentials

Sarmistha Bhunia, Abhishek Dey, et al.

FEBRUARY 06, 2023

JOURNAL OF THE AMERICAN CHEMICAL SOCIETY

READ 🗹

Nanosecond Metal-to-Ligand Charge-Transfer State in an Fe(II) Chromophore: Lifetime Enhancement via Nested Potentials

Justin T. Malme, Josh Vura-Weis, et al.

MARCH 13, 2023

JOURNAL OF THE AMERICAN CHEMICAL SOCIETY

READ 🗹

Triarylamine-Substituted Benzimidazoliums as Electron Donor-Acceptor Dyad-Type Photocatalysts for Reductive Organic Transformations

Ryo Miyajima, Eietsu Hasegawa, et al.

MAY 01, 2023

JOURNAL OF THE AMERICAN CHEMICAL SOCIETY

READ 🗹

Get More Suggestions >